Composition and Structure of Fluorescent Graphene Quantum Dots Generated by Enzymatic Degradation of Graphene Oxide

Xiaoyun He,[†] *Dan C. Sorescu,*[‡,§] *Alexander Star*[†,||,]*

[†]Department of Chemistry, University of Pittsburgh, Pittsburgh, Pennsylvania 15260, United States

[‡]United States Department of Energy, National Energy Technology Laboratory, Pittsburgh, Pennsylvania 15236, United States

[§]Department of Chemical and Petroleum Engineering, University of Pittsburgh, Pittsburgh, Pennsylvania 15261, United States

[||]Department of Bioengineering, University of Pittsburgh, Pittsburgh, Pennsylvania 15261, United States

*Corresponding author email: astar@pitt.edu

Keywords: fluorescent polyaromatic hydrocarbons, liquid chromatography, mass spectrometry, composition and structure screening, enzymatic degradation

Abstract

The wide applications of carbon nanomaterials (CNMs) in both materials and life sciences necessitate investigation of their metabolites due to the inevitable contact of CNMs and biological systems. Graphene oxide (GO), along with other types of CNMs, can be enzymatically degraded by myeloperoxidase (MPO), an enzyme released during the innate immune response. However, the enzymatic degradation products are neither well-defined nor well-understood. Some products generated during MPO-catalyzed degradation of GO could emit blue photoluminescence (PL) and were simply dubbed graphene quantum dots (GQDs) without further elucidating their structures. In this work, we use liquid chromatography-mass spectrometry (LC-MS) to isolate and elucidate chemical structures of the MPO-catalyzed degradation products. A general chemical formula screening workflow was developed for the GQDs, which are in the form of polyaromatic hydrocarbons (PAHs), obtained in the degradation products. Structures of the PAHs responsible for the blue PL were further proposed using density functional theory (DFT) calculations. Our results indicated that structures with several conjugated benzene rings are likely to generate the observed PL. This work provides insights into the mechanism of enzymatic degradation and open opportunities for fluorescence imaging of GO in biological systems.

Introduction

Carbon nanomaterials (CNMs) such as carbon nanotubes and graphene have attracted tremendous attention for various applications in multiple fields including energy conversion and storage,[1, 2] chemical sensors, and biomedicine.[3] However, increasing use of CNMs also necessitates careful scrutiny of their impact on biological systems and human health. Understanding their interactions with cells of the innate immune system is of particular importance.[4-6] Myeloperoxidase (MPO), a key enzyme released by neutrophils during inflammation, has been shown to catalyze the biodegradation of carbon nanomaterials both *in vitro* and *in vivo*.[7, 8] Specifically, Kagan *et al*.[9] reported that incubation of carboxylated single-walled carbon nanotubes (SWCNTs) with MPO, H_2O_2, and Cl^- results in degradation into a series of carbonaceous by-products including but not limited to CO, CO_2, and a range of hydrocarbons. Kurapati *et al.*[10] have reported biodegradation of graphene oxide (GO) sheets by MPO in the presence of 200 μM H_2O_2. *In vitro* oxidation of GO by neutrophils has also been investigated and the generated degradation products have been found to be non-genotoxic.[11] However, the intermediate degradation products were hypothesized to be polycyclic aromatic hydrocarbons (PAHs) (Figure 1) with well-documented toxicity on their own.[12] Therefore, investigation of the oxidative biodegradation of CNMs and identification of their degradation products is of upmost importance to biological health.

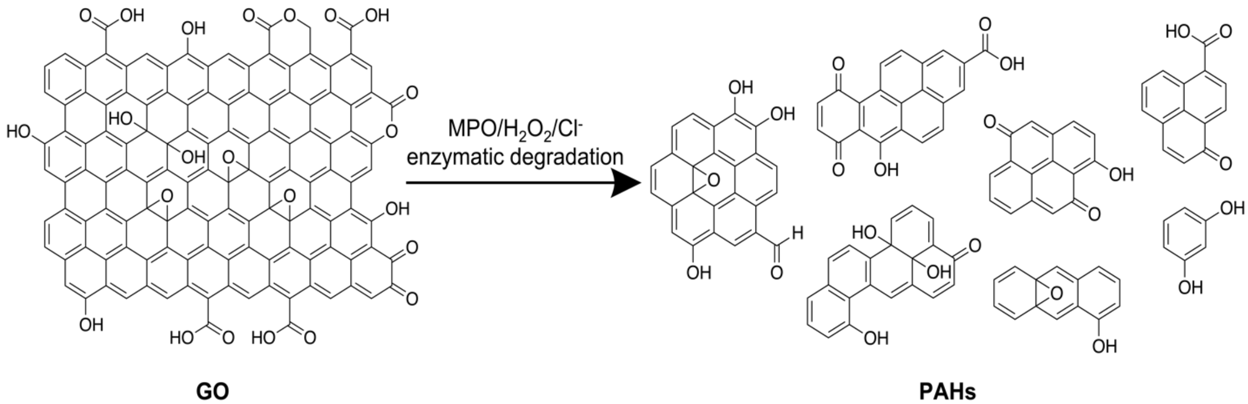

Figure 1. Schematic diagram illustrating the oxidative biodegradation of graphene oxide (GO) into polycyclic aromatic hydrocarbons (PAHs).

We have recently reported the observation of gradually increased photoluminescence (PL) of GO during MPO-catalyzed enzymatic degradation.[13] We attributed the observed fluorescence to the formation of the fluorescent degradation products, graphene quantum dots (GQDs)[14, 15] or carbon quantum dots,[16] which are presumably PAHs with specific molecular structures. Similar blue-luminescent GQDs have also been previously generated through a photo-Fenton oxidation reaction of GO.[14, 17] Although some of the CNMs oxidative products generated through both enzymatic degradation[9, 18] and photo-Fenton reaction[14, 17] have been identified, the assigned products were found to be non-fluorescent in nature. The newly demonstrated PL property of the degradation products provide spectroscopic information that can help into structure assignment, as it implies certain energy bandgap between the highest occupied molecular orbital (HOMO) and the lowest unoccupied molecular orbital (LUMO). Therefore, in this work, we performed a composition and structure screening of the formed fluorescent PAHs by liquid chromatography-mass spectrometry (LC-MS) and density functional theory (DFT) calculations. By correlating the assigned products to the observed blue PL, our results would be helpful to understand the origin of fluorescent GO degradation products and contribute to future applications of GO in PL bio-imaging.

Materials and Methods

Similar to the reported MPO-catalyzed oxidation of CNMs,[9, 11] MPO enzymatic degradation of GO was conducted as described previously.[13] Samples were prepared by adding 446 μL 1× phosphate buffer saline (PBS) (Sigma-Aldrich, 0.01 M phosphate buffer, 0.0027 M potassium chloride and 0.137 M sodium chloride, pH 7.4, at 25°C) and 50 μL of 1 mg/mL GO. Lyophilized MPO (Athens Research & Technology, Inc.) was dissolved in 1× PBS with a final concentration of 2.5 μg/μL and added to all six vials at a volume of 2 μL. MPO/H_2O_2/Cl^- degradation was activated by adding 2 μL 25 mM H_2O_2 (Fisher Scientific) every hour, for a total of seven additions per day for 5 days. 2 μL MPO were replenished daily to compensate for the loss. For control MPO experiments without GO, equal volumes of nanopure H_2O were added to the reaction mixture as a substitute for GO. It should be noted that as the MPO will gradually deactivate during incubation and H_2O_2 additions; seven additions of H_2O_2 were considered within 6 hours to ensure an efficient oxidation. Besides, as higher concentrations of H_2O_2 will deactivate MPO faster,[19] H_2O_2 was added in the seven aliquots instead of one addition. It has also been previously reported that the acidification of the reaction mixture upon H_2O_2 addition is compatible with the enzyme activity during proposed degradation procedures.[11]

The oxidized products were collected by dichloromethane (DCM) extraction. After the DCM extraction, the solvent was evaporated and the resulting residue was resuspended in 500 μL of methanol for injection into the LC-MS column. It could be reasoned that GO degradation products, in the form of PAHs with extended π-conjugated systems, are preferably present in the organic DCM layer instead of the aqueous layer as a result of the difference in solubility.[15, 20] A similar extraction method has been used to analyze the enzymatic degradation products of SWCNTs.[18]

Liquid chromatography (LC) was performed using a Dionex-Ultimate 3000 (Thermo Fisher Scientific). The column employed was a Hypersil Gold C18, 100 × 2.1 mm length and 1.9 μm particle size from Thermo Fisher Scientific. The mobile phases used were 0.1% formic acid in water (mp1) and 0.1% formic acid in acetonitrile (mp2). An isocratic program with 30% mp1 and 70% mp2 was used. The flow rate was held constant at 200 μL min^{-1} with an injection volume of 5 μL.

The LC effluent was pumped into a Q Exactive benchtop Orbitrap-based mass spectrometer (Thermo Fisher Scientific) with electrospray ionization (ESI) held at either positive or negative polarity. Nitrogen sheath gas and auxiliary gas flow rate were set up at 35 and 10 (arbitrary units), respectively. The capillary temperature was set at 250°C, the spray voltage was 3.5 kV and the S-lens voltage was set to 60 V. The instrument was operated at 70,000 resolving power and the automatic gain control (AGC) target was 1×10^6.

MS/MS (MS^2) spectra were acquired by data dependent MS^2 experiments with an applied fragmentation energy of 30 eV. The experiments were operated at 35,000 resolving power. The AGC target and the maximum ion injection time (IT) were set to 1E5 and 50 ms.

The absorption and emission spectra of molecular systems of interest were calculated using time-dependent DFT[21-23] for the ground and excited states as implemented in Gaussian 16 package.[24] Calculations were performed at CAM-B3LYP/6-311+G(2d,p) level of theory.[25] The effect of bulk solvent (water) on molecular configurations and on the corresponding vertical excitation and emission energies was considered by means of a polarizable continuum model[26, 27] with inclusion of state-specific solvation for absorption or emission. An ultrafine integration grid with 99 radial shells and 590 angular points per shell was used in all calculations.

Results and Discussion

Figure 2 displays the LC-MS total ion chromatogram (TIC) profile in positive ionization mode of three different samples corresponding to pure methanol, MPO control, and degradation products after 5-

day MPO/H_2O_2/Cl^- oxidation of GO. Similar chromatography peaks at retention time ~1 min appeared across all three samples, showing the background chromatographic peak. In contrast to the first two samples (Figures 2a and 2b), the chromatograph of the third sample (Figure 2c) displayed additional late-eluted chromatography peaks, indicating that these peaks could be a result of the formed GO degraded products. It can be reasoned that compared with solvent (methanol) and non-GO related products, such as dityrosine,[28, 29] formed in the MPO control sample, GO oxidative products with original π-conjugated systems would exhibit higher hydrophobicity and would have longer retention time.

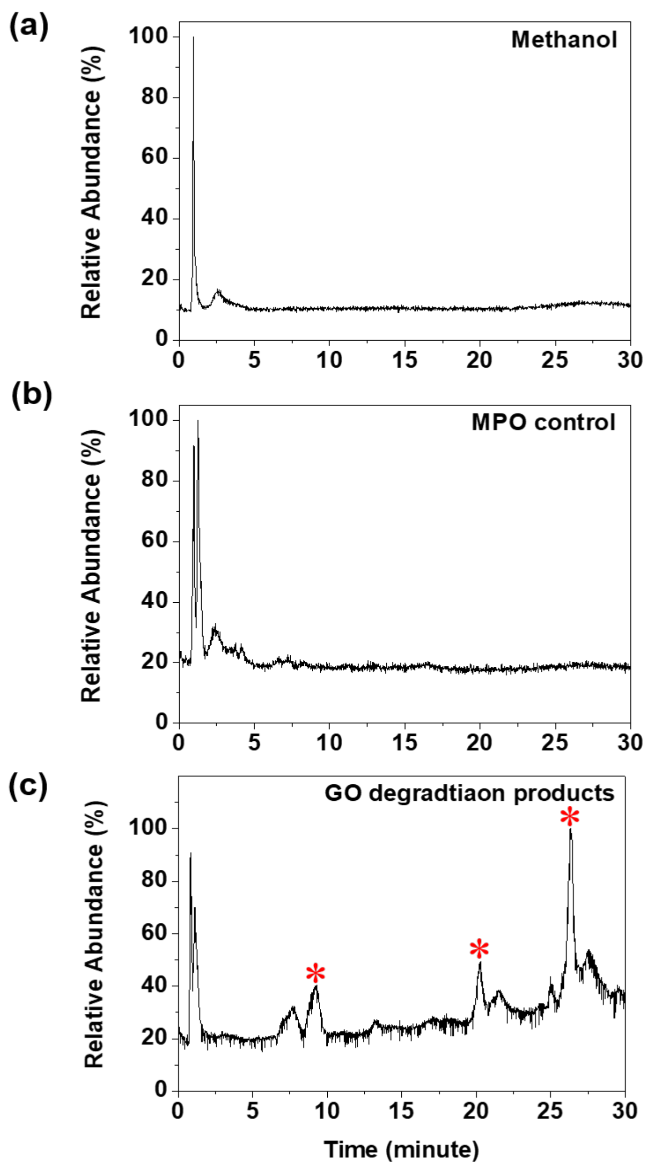

Figure 2. LC-MS total ion liquid chromatograms (TIC) in positive ionization mode of (a) pure methanol, (b) MPO control, and (c) after 5-day MPO/H_2O_2/Cl^- degradation of GO. Note: the red * symbol in panel (c) indicates the peak subjected to chemical formula screening.

In order to search for the potential molecular ion peaks correlated with GQDs, i.e., the generated PAHs degradation products, we focused on three fractions eluted at 9.28 min, 20.29 min, and 26.35 min (denoted using a red * symbol in Figure 2c). Figure S1 displays the positive ion electrospray ionization (ESI) mass spectra obtained for the selected peaks. Here, a non-target screening workflow (Figure 3) was developed to filter out the chemical composition for the tentative GQDs, which are in the form of PAHs, in the degradation products. First, only the molecular ion peaks with relative intensities higher than 1% were chosen for analysis (Step I). At the same time, the relative intensity of the selected molecular ion peaks should be less than 1% in both pure methanol and in MPO control samples, as potential contributions from degradation products should not be present in both samples. After filtering out potential molecular ion peaks based on the 1% threshold cutoff, the following criteria were implemented to assign possible chemical compositions for each selected peak. Limit the number and type of elements (Step II) to ^{12}C (up to 100), ^{1}H (up to 100), ^{16}O (up to 100), ^{23}Na, ^{39}K, and ^{14}N (one ^{23}Na, ^{39}K, and ^{14}N for a singly charged peak, two ^{23}Na, ^{39}K, and ^{14}N for a doubly charged peak, and so forth). Also, the ideal composition candidates must contain at least three elements, *i.e.*, C, H and O. Different from laser desorption ionization (LDI) and/or matrix-assisted laser desorption ionization (MALDI) ionization methods, which produce primarily singly charged ions,[30-33] ESI could generate a range of multiply charged species[34] for each molecule: +2, +3, +4 and so on. Moreover, as ESI is one of the softest ionization techniques, detectability of some adducts during the ESI process depends on the availability of the small ions in the analytical process.[35, 36] For example, sodium is one of the most common impurity, which could arise from multiple sources such as mobile phase additives, solvents, glassware, and so on.[37, 38] Therefore, sodium adducts could be formed during the MS analysis. Here, four types of cationic adducts, namely $[M + nH]^{n+}$, $[M + nNa]^{n+}$, $[M + nK]^{n+}$, and $[M + nNH_4]^{n+}$, were taken into consideration, where M represents the volatile analyte neutral molecules. The mass errors of the generated composition candidates for each molecular ion peak should be within ± 5 ppm (Step III). The ring double bond (RDB) value in the molecular candidates should be ≥4 to ensure the presence of at least one benzene ring in the structures (Step IV). The difference between experimental and theoretical intensity ratio of M+1(0.5) (isotope peak, 1 and 0.5 are the isotopic spacing for singly and doubly charged base peak, respectively) and M (base peak) should be within ±10 % (Step V).

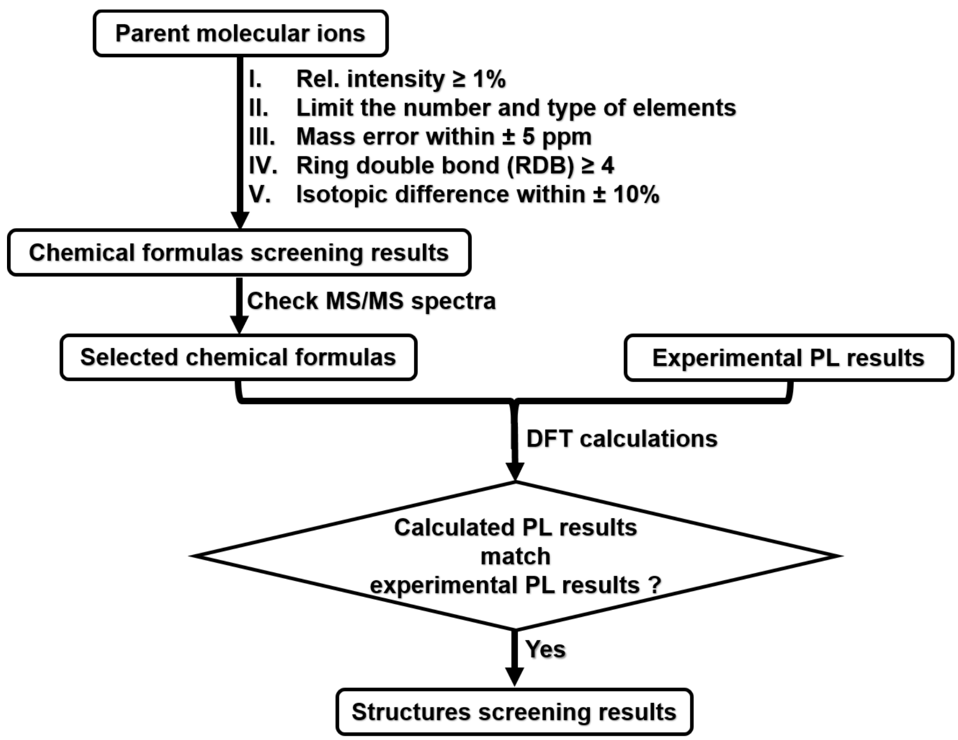

Figure 3. Workflow for chemical formula and structure screening of potential PAHs generated through enzymatic degradation of GO.

All the peaks that met the aforementioned criteria are summarized in Table S1. Four types of oxygen functionalities are known to exist in the GO: epoxide, hydroxyl, carbonyl, and carboxyl groups.[39] While epoxide and carbonyl groups are expected to be detected in the positive ESI mode, hydroxyl and carboxyl groups are less sensitively detected in this positive mode.[40, 41] Therefore, a chemical formula screening for the peaks detected in negative ionization mode (Figures S2 and S3) has also been performed using a procedure similar to that described in Figure 3 and the corresponding results are summarized in Table S2. In the negative-ion mode, deprotonated $[M - H]^-$ and $[M + Cl]^-$ adducts were taken into consideration. Therefore, in Step II, four types of elements, ^{12}C, ^{1}H, ^{16}O and ^{35}Cl, were allowed. The maximum number of ^{12}C, ^{1}H, and ^{16}O atoms remained 100, respectively, while the upper limit for maximum number of ^{35}Cl is one for a singly charged peak, two for a doubly charged peak, and so forth. Taken together the chemical formula screening results obtained in both positive and negative ionization modes are presented in Tables S1 and S2, respectively. The molecular weight of all the filtered GO biodegradation products ranged from ~150 to ~ 780 Da. They contained 7 to 50 carbon atoms, 4 to 80 hydrogen atoms, and 1 to 13 oxygen atoms. The carbon to oxygen (C/O) ratio varied from 1.4 to 25, comparable to the reported values of graphene-based material with different extent of oxidation.[42-44]

On the basis of the above chemical formula screening results, we proposed a mechanism of the $MPO/H_2O_2/Cl^-$ enzymatic degradation of GO and generation of PAHs as described in Scheme 1. Here, hypochlorite (ClO^-) and reactive radical intermediates of MPO are the two oxidants involved in biodegradation of GO.[9, 13, 45] These two strong oxidants could play a similar role as the one reported for hydroxyl radicals.[14] They start attacking the defect sites in GO, namely those sp^3 carbon atoms connected with hydroxyl and epoxide groups on the basal planes to break the C-C/C=C bonds apart (Scheme 1). Epoxide groups present on the basal planes of GO are particular unstable due to the unfavorable ring strain.[46] Additionally, carbonyl groups can also interact with ClO^-.[45] The oxidation procedure is evidenced by an increase in the oxidation state of carbon atoms (highlighted in red in Scheme 1). Specifically, in the starting GO structures, the oxidation state of the hydrogenated sp^2 edge carbon atom is –1, while the oxidation state of the in-plane sp^3 carbon connected with hydroxyl group is +1. During the enzymatic oxidation, the oxygen-containing functional groups can undergo further oxidation, such that the oxidation state of the carbon atom increases to +2, and further to +4 in the case of CO_2. In these processes, different carbon-carbon bonds break thus effectively generating small sp^2 conjugated domains (usually less than 100 nm in size) in the form of PAHs that are free to fluoresce. The edges of the generated aromatic molecules should be either (partially or fully) hydrogenated or contain some oxygen functional groups. In addition, the following two processes are expected to happen during the entire degradation. First, similar to the case of carbon nanotubes,[47, 48] it is anticipated that ClO^- could generate carboxyl and hydroxyl groups on the GO, which may serve as new degradation active sites, or ClO^- can form epoxides from terminal olefins.[49] Second, it is assumed that decarboxylation of carboxylic acid groups with formation of CO_2 could take place throughout the enzymatic oxidation.[45]

The proposed structural changes (Scheme 1) occurring during the enzymatic reaction have been evidenced by transmission electron microscopy (TEM, Figure S4) and Raman spectroscopy (Figure S5). Micrometer-sized GO completely disappeared after 5-days of enzymatic oxidation treatment leading to nanometer-sized degradation products (Figure S4b). The Raman spectrum of the pristine GO displays two characteristic D and G peaks, which are assigned to the sp^3 and sp^2 bonding states, respectively.[50] Both peaks significantly decreased after 5-day enzymatic oxidation confirming the degradation of GO. The D- to G-band intensities ratio, I_D/I_G, increases from 1.18 for pristine GO to 1.51 after enzymatic oxidation, indicating an increased disorder in the graphitic carbon lattice. It could be reasoned that while most of the oxygenated groups are removed during the degradation, the generation of the holes within the basal planes of GO leads to discontinuity of its long-range sp^2 domains and a corresponding increase in the I_D/I_G.[51]

The proposed mechanism can be further supported by X-ray photoelectron spectroscopy (XPS) results (Figure S6). The quantified carbon-to-oxygen (C/O) atomic ratio was calculated based on XPS survey scan shown in Figure S6a. The increase of C/O atomic ratio from 1.94 in GO to 5.39 after 5-day degradation confirms the consumption of the oxygen-containing functional groups during the enzymatic degradation. This result is in accordance with our assumption that the oxygen-containing functional groups serve as the initial reactive sites being attacked and leading to the break of their surrounding C-C/C=C bonds. It should be noted that during the enzymatic degradation process the products are inevitably subject to different degrees of oxidation, which would consequently lead to an inhomogeneous nature of the degradation products and various C/O ratios (Tables S1 and S2). While the C/O ratio of 5.39 for the degradation products acquired using XPS characterization was obtained under the assumption of homogeneous products, the obtained value is within the range of C/O ratios obtained based on composition screening results (Tables S1 and S2) as found in LC-MS measurements and thus could represent the averaged composition property of the products. High-resolution C 1s spectra (Figure S6b) were deconvoluted into four peaks with varied proportions, corresponding to C-C/C=C in aromatic rings, C-O groups, C=O groups, and π to π^* satellite peak. After 5-day degradation, a decrease in peaks associated with oxygenated carbon was observed. The increased contribution of C-C/C=C species, compared to oxygenated carbon species as seen in C 1s spectra is also consistent with the increase of C/O atomic ratio, demonstrating that the degraded products are less oxidized. The π-π* satellite peak has been noticed for different chemically reduced GOs evolved upon chemical reduction of GO.[52, 53] The appearance of π-π* satellite contribution in the 5-day degradation products implies that the delocalized π-conjugated system was restored during the enzymatic degradation process.

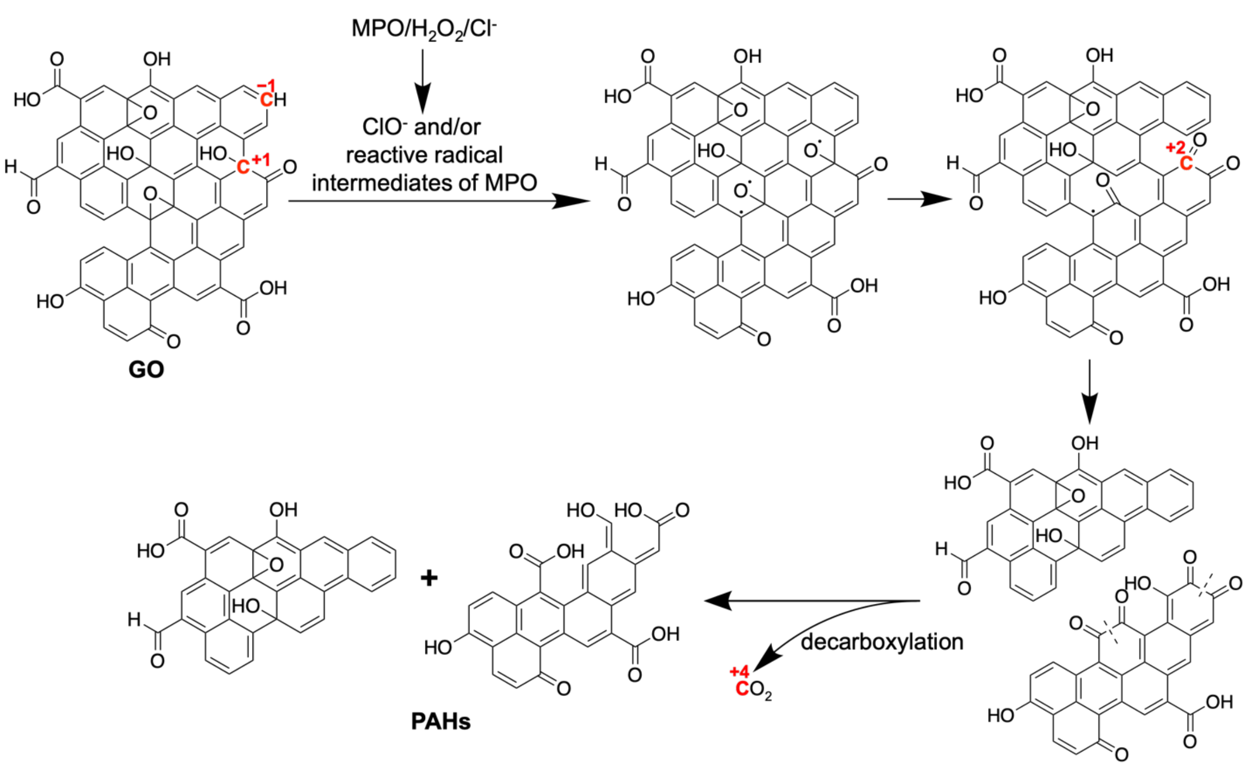

Scheme 1. Schematic representation of the proposed mechanism for $MPO/H_2O_2/Cl^-$ degradation of GO. The numbers indicated in red correspond to oxidation state of the carbon atoms.

Next, we focused on a more in-depth characterization of the obtained PAHs systems in terms of the chemical formula screening results (Tables S1 and S2). For this purpose, we have considered the case of molecular ions with specific mass-to-charge ratios m/z of 485.11 and 251.04 (Table 1), eluted at a retention time of 26.35 min in the positive-ion mode. In contrast to other ions that can be fragmented and can lead to diverse fragmentation patterns (Figures S7-S18, data for other peaks were not shown), the two molecular ions indicated above can be hardly fragmented during ionization process as shown in LC-MS/MS product ion spectra (Figures 4a and 5a). As a result, it can be assumed that these two molecular ions have relative compact structures and contain extended conjugated π systems (Figure 4b and 5b), making them less susceptible to fragmentation. For these two ions, chemical formulas with the lowest mass error (Table 1), namely $C_{33}H_{18}O_3$ and $C_{25}H_{18}O_{10}$, were chosen. It should be noted that neither the extra hydrogen nor the sodium atoms (Figures 4b and 5b) attached to the proposed structures (with formula $C_{33}H_{18}O_3$ and $C_{25}H_{18}O_{10}$) are from the degradation product sample itself. The formation of either hydrogen or sodium cation adducts during the LC-MS analysis is due to the soft ESI ionization process as aforementioned.

Table 1. Possible PAHs generated by $MPO/H_2O_2/Cl^-$ oxidation of GO.

Mass to charge ratio (m/z)	Experimental M+1(0.5)/M (%)	Charge (z)	Chemical formula	RDB[a]	Mass error (ppm)	Theoretical M+1(0.5)/M (%)
485.11378	39.93	1	$[C_{33}H_{18}O_3 + Na]^+$	25	–2.13	35.69
			$[C_{30}H_{22}O_4 + K]^+$	20	–2.45	32.45
251.04363	36.14	2	$[C_{25}H_{18}O_{10} + H + Na]^{2+}$	17	1.52	27.04
			$[C_{27}H_{16}O_{10} + 2H]^{2+}$	20	–3.27	29.2

[a] RDB = ring double bond.

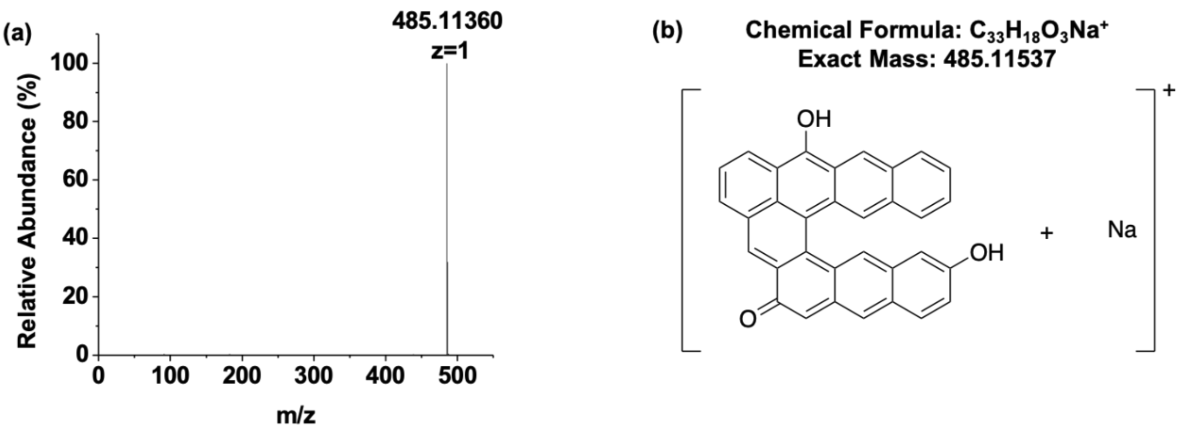

Figure 4. (a) LC-MS/MS product ion spectrum of the precursor ion m/z 485.11 in Table 1. (b) Tentative structure assignment.

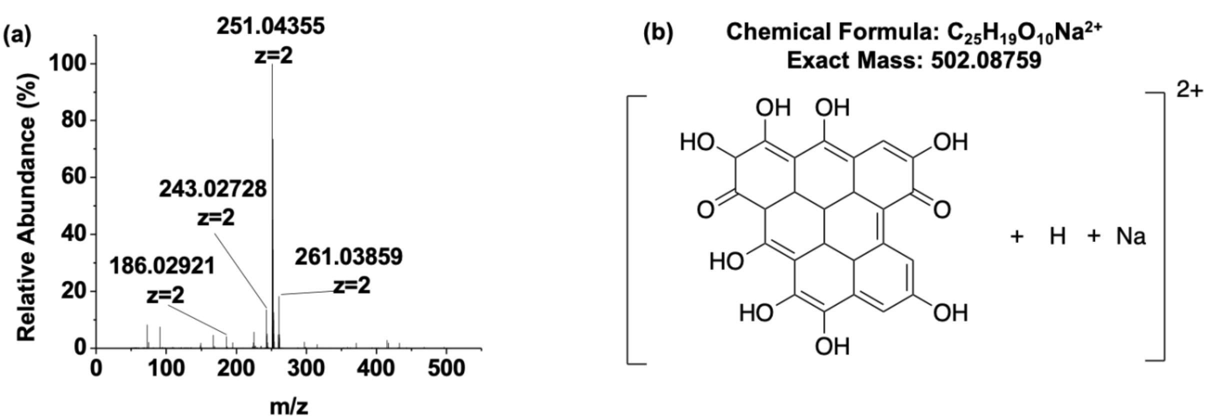

Figure 5. (a) LC-MS/MS product ion spectrum of the precursor ion m/z 251.04 in Table 1. (b) Tentative structure assignment.

For the resulted GO enzymatic degraded products, we have also performed an analysis of their fluorescence properties. Specifically, we found[13] that under 325 nm excitation, the degradation products have a blue fluorescence emission at 440 nm as shown in Figure S19. These spectroscopic findings impose additional electronic requirements that can be used in a structural screening process.

The information obtained from LC-MS and photoluminescence experiments has been further used to perform a theoretical screening of different molecular structures. The fundamental objective of this screening stage was to investigate if molecular systems having the same stoichiometries as those obtained in LC-MS experiments can be also responsible for the observed photoluminescence, showing in particular a blue photoluminescence in the 440 nm region under a 325 nm excitation. The structural screening has been initiated starting from the two stoichiometries $C_{33}H_{18}O_3$ and $C_{25}H_{18}O_{10}$, hereafter denoted as A and B, identified in our LC-MS experiments. Despite the apparent simplicity of these two sets of compounds, the associated chemical space of possible structural forms having these two stoichiometries is very large. In order to reduce the range of possibilities we followed a procedure consistent to the one described above for analysis of LC-MS data. Specifically, for the two A and B sets, we analyzed only the case of compact structures composed primarily from aromatic carbon rings with a high fraction of sp^2 hybridized carbon atoms. One might assume that upon enzymatic degradation, the resulted graphitic structures are primarily composed of 6-membered carbon rings but we included also the possibility that the resulted polycyclic aromatic systems can contain at most one 5- or 7-membered ring. Consistent to experimental findings, the edges of the structures are hydrogenated or contain oxygen functional groups consistent to those observed experimentally and satisfy the requirement to present ionization in a positive-ion mode. For the structures tested we have performed optimizations of the ground and electronic excited states under solvation conditions and determined the associated excitation and luminescence energies. The final selected molecular configurations have the experimentally derived stoichiometries and present UV absorption in the energy range (325 ± 20) nm and blue luminescence in the spectral range (440 ± 20) nm, consistent to our experimental results. The ± 20 nm spread range for either absorption or emission is somewhat arbitrary and represents an estimated uncertainty interval motivated both by errors inherent to our PL experiments, for example due to selection of a 10 nm slit width, as well as by differences in spectral deviations related to the phosphate buffer saline solvent used in our experiments vs a pure water solvent used in computations. We also note that the solvent has been described in our theoretical analysis using of a polarizable continuum model[26, 27] and such a description might not fully incorporate the complexity of real solvent clusters that might be formed at the interface with various functional oxygen groups decorating the PAHs structures.

In Figure 6 we summarize molecular configurations for compounds with A and B stoichiometries having absorption and fluorescence lines in the spectral ranges of interest. Additional details related to the specific electronic transitions involved in each case are detailed in Table S4. In Figure 6, A1-A3 and B1-B3 compounds represent systems which satisfy the general requirements imposed based on our experimental data in terms of compound stoichiometry, namely the need to be formed exclusively from 6-membered rings, to have a compact structure less susceptible to fragmentation, to have the expected oxygen or hydrogen functional groups decorating the edge carbon sites and to be characterized by optical absorption and emission energies consistent to our experimental PL measurements. Beside these systems we show that other type of molecular structures are also possible, for example compounds composed primarily from 6-membered carbon rings with one additional 5-membered ring (A4-A6, A8, A9) or a 7-membered ring (A7). Moreover, in addition to hydroxyl functional group, the systems can be decorated with ester, ether (epoxide), and/or carbonyl groups. A full list of the set of molecular configurations identified containing these groups are provided in Table S4. In addition, in Table S5 we indicate structures containing purely hydroxyl or a mixture of hydroxyl and carboxylic groups, while satisfying the same spectroscopic limitations. Though hydroxyl and carboxyl groups are less sensitive, compared to the epoxide and carbonyl groups, to be detected in the positive ionization mode, the proposed structures shown in Table S5 are still of interest as hydroxyl and carboxyl groups could be major components in some of the degradation PAHs products.

Overall, the above results demonstrate that within the two general stoichiometries A ($C_{33}H_{18}O_3$) and B ($C_{25}H_{18}O_{10}$) identified by LC-MS measurements in the enzymatic degradation of GO, several different types of polycyclic hydrocarbon compounds having a high fraction of sp^2/sp^3 hybridized carbon and emitting blue light when excited with UV radiation can be identified, consistent to experimental results performed in this study.

A similar blue PL to the one found in this study has been reported previously in the case of chemically derived graphene oxide using hydrazine as a reducing agent.[54] In that study, the absorbance was found to increase with hydrazine exposure time, leading to a PL intensity correlated to the amount of small sp^2 clusters formed. In particular, it was suggested[54] that very small clusters containing only few aromatic rings should be responsible for the observed blue PL. The results reported in the current work as indicated in Figure 6 fully support these previous expectations and demonstrate that indeed, small sp^2 clusters containing only several (<10) aromatic rings, can present blue emission as observed experimentally. In contrast, based on the fact that the width of benzene is ~ 2.8 Å,[55] the nm-sized degradation products observed under transmission electron microscopy (TEM, Figure S4b) could consist ~ 8000 benzene rings (for a ~ 20 nm particle), which make them less likely be responsible for the blue PL. In addition, using computational calculations, it was observed that in general the band gap of PAHs decreased as the particle size increased.[16, 56, 57] The energy gap is ~ 7 eV for a single benzene molecule and decreases to about 2 eV for systems containing about 20 aromatic rings.[54, 58] Therefore, given the size of the observed carbonaceous degradation products, the corresponding gap is estimated to be too small to generate blue PL.

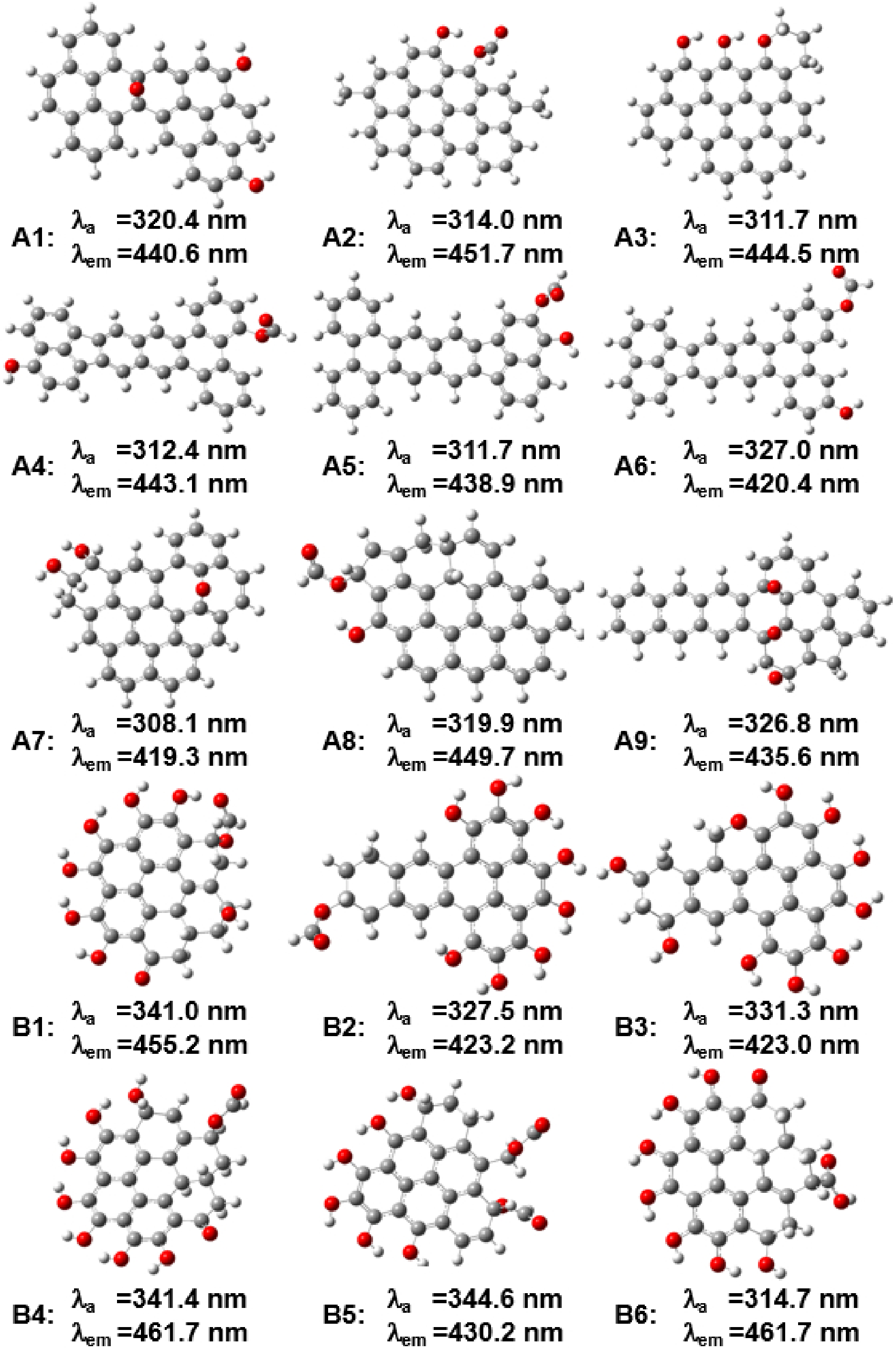

Figure 6. Molecular configurations with (A) $C_{33}H_{18}O_3$ and (B) $C_{25}H_{18}O_{10}$ stoichiometries. For each system the corresponding absorption vertical excitations (in the range (325 ± 20) nm) and fluorescence energies are indicated. The color scheme corresponds to C (gray), H (white) and O (red).

Compared with low-molecular-weight PAHs containing two or three rings which occur in the atmosphere, predominantly in the vapor phase, the above identified fluorescent products in the form of multi-ringed PAHs (containing more than four rings) could largely bound to particles and are in particulate phase.[59] As majority of the high-molecular-weight PAHs are identified as carcinogenic,[60, 61] similar to the reported DNA damage effect in the lung carcinoma cells of the enzyme-oxidized SWCNTs,[62] the bioaccumulation of the proposed fluorescent products from enzymatic degradation of GO could have potential toxicological concerns. Even though the GO oxidative products have been found to be non-genotoxic on bronchial epithelia cell line BEAS-2B,[11] other studies have shown that the toxicology of PAHs can depend on several factors including its functional groups,[63] size,[12] dose,[64] and metabolic activation.[65, 66, 67]

Conclusion

In this work, we investigated the chemical compositions of the enzymatic oxidative products of GO, using LC-ESI-Orbitrap MS with up to 70,000 resolving power. A non-target screening workflow was developed to filter out the specific chemical formulas for the tentative PAHs products. The structures of the PAHs were proposed based on a combined use of experimental fluorescence measurements and DFT calculations. We demonstrated that polycyclic aromatic structures containing few conjugated repeating benzene units could be responsible for the observed blue PL emission. These results provide additional insight into the origin of fluorescence in GO enzymatic degradation, and can be used also as a practical method for tracking GO degradation products in biosensing and fluorescence tagging applications. The developed chemical composition and structure screening workflow could also be applicable to investigate the fluorescence origins of GQDs generated through other oxidation methods than the enzymatic degradation considered in this work.

Associated Content

Supporting Information

Additional Methodological Details; positive-ion and negative-ion ESI mass spectra of selected chromatographic peaks; potential PAHs generated by $MPO/H_2O_2/Cl^-$ oxidation of GO (detected in both positive and negative ionization modes); LC-MS TIC in negative ionization mode; TEM, Raman, XPS, and PL spectra of GO and GO after 5-day $MPO/H_2O_2/Cl^-$ degradation; LC-MS/MS ion chromatograms showing the product ion profiles and LC-MS/MS product ion spectra of the precursor ions at retention time of 26.35 min in Table S1; comparison of PL emission under different excitations of GO after 5-day MPO-catalyzed degradation; additional details related to the DFT proposed structures.

Acknowledgement

The work at the University of Pittsburgh was supported by the National Science Foundation under grant no. 2003302. We thank the Nanoscale Fabrication and Characterization Facility (NFCF) and the Mass Spectrometry Lab at the University of Pittsburgh for access to the characterization instrumentation. We especially thank Bhaskar Godugu for help provided during sample and data analysis.

References

1. Dai, L.; Chang, D. W.; Baek, J.-B.; Lu, W. Carbon Nanomaterials for Advanced Energy Conversion and Storage. *Small* **2012,** *8*, 1130-1166.

2. Zhang, J.; Xia, Z.; Dai, L. Carbon-based electrocatalysts for advanced energy conversion and storage. *Sci. Adv.* **2015,** *1*, e1500564.

3. Loh, K. P.; Ho, D.; Chiu, G. N. C.; Leong, D. T.; Pastorin, G.; Chow, E. K.-H. Clinical Applications of Carbon Nanomaterials in Diagnostics and Therapy. *Adv. Mater.* **2018,** *30*, 1802368.

4. Fadeel, B.; Bussy, C.; Merino, S.; Vázquez, E.; Flahaut, E.; Mouchet, F.; Evariste, L.; Gauthier, L.; Koivisto, A. J.; Vogel, U.; *et al*. Safety Assessment of Graphene-Based Materials: Focus on Human Health and the Environment. *ACS Nano* **2018,** *12*, 10582-10620.

5. Kobayashi, N.; Izumi, H.; Morimoto, Y. Review of toxicity studies of carbon nanotubes. *J. Occup. Health* **2017,** *59*, 394-407.

6. Madannejad, R.; Shoaie, N.; Jahanpeyma, F.; Darvishi, M. H.; Azimzadeh, M.; Javadi, H. Toxicity of carbon-based nanomaterials: Reviewing recent reports in medical and biological systems. *Chem.-Bio. Interact.* **2019,** *307*, 206-222.

7. Kotchey, G. P.; Hasan, S. A.; Kapralov, A. A.; Ha, S. H.; Kim, K.; Shvedova, A. A.; Kagan, V. E.; Star, A. A natural vanishing act: the enzyme-catalyzed degradation of carbon nanomaterials. *Acc. Chem. Res.* **2012,** *45*, 1770-1781.

8. Vlasova, I. I.; Kapralov, A. A.; Michael, Z. P.; Burkert, S. C.; Shurin, M. R.; Star, A.; Shvedova, A. A.; Kagan, V. E. Enzymatic oxidative biodegradation of nanoparticles: Mechanisms, significance and applications. *Toxicol. Appl. Pharmacol.* **2016,** *299*, 58-69.

9. Kagan, V. E.; Konduru, N. V.; Feng, W.; Allen, B. L.; Conroy, J.; Volkov, Y.; Vlasova, I. I.; Belikova, N. A.; Yanamala, N.; Kapralov, A.; *et al*. Carbon nanotubes degraded by neutrophil myeloperoxidase induce less pulmonary inflammation. *Nat. Nanotechnol.* **2010,** *5*, 354-359.

10. Kurapati, R.; Russier, J.; Squillaci, M. A.; Treossi, E.; Ménard-Moyon, C.; Del Rio-Castillo, A. E.; Vazquez, E.; Samorì, P.; Palermo, V.; Bianco, A. Dispersibility-Dependent Biodegradation of Graphene Oxide by Myeloperoxidase. *Small* **2015,** *11*, 3985-3994.

11. Mukherjee, S. P.; Gliga, A. R.; Lazzaretto, B.; Brandner, B.; Fielden, M.; Vogt, C.; Newman, L.; Rodrigues, A. F.; Shao, W.; Fournier, P. M.; *et al*. Graphene oxide is degraded by neutrophils and the degradation products are non-genotoxic. *Nanoscale* **2018,** *10*, 1180-1188.

12. Haritash, A. K.; Kaushik, C. P. Biodegradation aspects of Polycyclic Aromatic Hydrocarbons (PAHs): A review. *J. Hazardous Mater.* **2009,** *169*, 1-15.

13. He, X.; White, D. L.; Kapralov, A. A.; Kagan, V. E.; Star, A. Photoluminescence Response in Carbon Nanomaterials to Enzymatic Degradation. *Anal. Chem.* **2020,** *92*, 12880-12890.

14. Zhou, X.; Zhang, Y.; Wang, C.; Wu, X.; Yang, Y.; Zheng, B.; Wu, H.; Guo, S.; Zhang, J. Photo-Fenton Reaction of Graphene Oxide: A New Strategy to Prepare Graphene Quantum Dots for DNA Cleavage. *ACS Nano* **2012,** *6*, 6592-6599.

15. Shinde, D. B.; Pillai, V. K. Electrochemical Resolution of Multiple Redox Events for Graphene Quantum Dots. *Angew. Chem. Int. Ed.* **2013,** *52*, 2482-2485.

16. Li, H.; He, X.; Kang, Z.; Huang, H.; Liu, Y.; Liu, J.; Lian, S.; Tsang, C. H. A.; Yang, X.; Lee, S.-T. Water-Soluble Fluorescent Carbon Quantum Dots and Photocatalyst Design. *Angew. Chem. Int. Ed.* **2010,** *49*, 4430-4434.

17. Bai, H.; Jiang, W.; Kotchey, G. P.; Saidi, W. A.; Bythell, B. J.; Jarvis, J. M.; Marshall, A. G.; Robinson, R. A. S.; Star, A. Insight into the Mechanism of Graphene Oxide Degradation via the Photo-Fenton Reaction. *J. Phys. Chem. C* **2014,** *118*, 10519-10529.

18. Allen, B. L.; Kotchey, G. P.; Chen, Y.; Yanamala, N. V. K.; Klein-Seetharaman, J.; Kagan, V. E.; Star, A. Mechanistic Investigations of Horseradish Peroxidase-Catalyzed Degradation of Single-Walled Carbon Nanotubes. *J. Am. Chem. Soc.* **2009,** *131*, 17194-17205.

19. Huang, J.; Smith, F.; Panizzi, J. R.; Goodwin, D. C.; Panizzi, P. Inactivation of myeloperoxidase by benzoic acid hydrazide. *Arch. Biochem. Biophys.* **2015,** *570*, 14-22.

20. Russo, C.; Apicella, B.; Ciajolo, A. Blue and green luminescent carbon nanodots from controllable fuel-rich flame reactors. *Sci. Rep.* **2019,** *9*, 14566.

21. Furche, F.; Ahlrichs, R. Adiabatic time-dependent density functional methods for excited state properties. *J. Chem. Phys.* **2002,** *117*, 7433-7447.

22. Scalmani, G.; Frisch, M. J.; Mennucci, B.; Tomasi, J.; Cammi, R.; Barone, V. Geometries and properties of excited states in the gas phase and in solution: Theory and application of a time-dependent density functional theory polarizable continuum model. *J. Chem. Phys.* **2006,** *124*, 094107.

23. Casida, M. E. Time-dependent density-functional theory for molecules and molecular solids. *J. Mol. Struct.: THEOCHEM* **2009,** *914*, 3-18.

24. Frisch, M. J.; Trucks, G. W.; Schlegel, H. B.; Scuseria, G. E.; Robb, M. A.; Cheeseman, J. R.; Scalmani, G.; Barone, V.; Petersson, G. A.; Nakatsuji, H.; *et al*. *Gaussian 16 Rev. C.01*, Wallingford, CT, 2016.

25. Yanai, T.; Tew, D. P.; Handy, N. C. A new hybrid exchange–correlation functional using the Coulomb-attenuating method (CAM-B3LYP). *Chem. Phys. Lett.* **2004,** *393*, 51-57.

26. Tomasi, J.; Mennucci, B.; Cammi, R. Quantum Mechanical Continuum Solvation Models. *Chem. Rev.* **2005,** *105*, 2999-3094.

27. Cancès, E.; Mennucci, B.; Tomasi, J. A new integral equation formalism for the polarizable continuum model: Theoretical background and applications to isotropic and anisotropic dielectrics. *J. Chem. Phys.* **1997,** *107*, 3032-3041.

28. Harms, G. S.; Pauls, S. W.; Hedstrom, J. F.; Johnson, C. K. Fluorescence and Rotational Dynamics of Dityrosine. *J. Fluoresc.* **1997,** *7*, 283-292.

29. Heinecke, J. W.; Li, W.; Daehnke, H. L.; Goldstein, J. A. Dityrosine, a specific marker of oxidation, is synthesized by the myeloperoxidase-hydrogen peroxide system of human neutrophils and macrophages. *J. Biol. Chem.* **1993,** *268* (6), 4069-4077.

30. Cazier, H.; Malgorn, C.; Fresneau, N.; Georgin, D.; Sallustrau, A.; Chollet, C.; Tabet, J.-C.; Campidelli, S.; Pinault, M.; Mayne, M.; *et al*. Development of a Mass Spectrometry Imaging Method for Detecting and Mapping Graphene Oxide Nanoparticles in Rodent Tissues. *J. Am. Soc. Mass Spectrom.* **2020,** *31*, 1025-1036.

31. Chen, S.; Xiong, C.; Liu, H.; Wan, Q.; Hou, J.; He, Q.; Badu-Tawiah, A.; Nie, Z. Mass spectrometry imaging reveals the sub-organ distribution of carbon nanomaterials. *Nat. Nanotechnol.* **2015,** *10*, 176-182.

32. Liu, Q.; Cheng, M.; Wang, J.; Jiang, G. Graphene Oxide Nanoribbons: Improved Synthesis and Application in MALDI Mass Spectrometry. *Chem. Eur. J.* **2015,** *21*, 5594-5599.

33. Jing, Z.; Hao-Yang, W.; Yin-Long, G. Amino Acids Analysis by MALDI Mass Spectrometry Using Carbon Nanotube as Matrix. *Chin. J. Chem.* **2005,** *23*, 185-189.

34. Hu, Q.; Meng, X.; Choi, M. M. F.; Gong, X.; Chan, W. Elucidating the structure of carbon nanoparticles by ultra-performance liquid chromatography coupled with electrospray ionisation quadrupole time-of-flight tandem mass spectrometry. *Anal. Chim. Acta* **2016,** *911*, 100-107.

35. Cech, N. B.; Enke, C. G. Practical implications of some recent studies in electrospray ionization fundamentals. *Mass Spectrom. Rev.* **2001,** *20*, 362-387.

36. Wang, C.; Wang, M.; Han, X. Applications of mass spectrometry for cellular lipid analysis. *Mol. BioSyst.* **2015,** *11*, 698-713.

37. Kruve, A.; Kaupmees, K.; Liigand, J.; Oss, M.; Leito, I. Sodium adduct formation efficiency in ESI source. *J. Mass Spectrom.* **2013,** *48*, 695-702.

38. Kruve, A.; Kaupmees, K. Adduct Formation in ESI/MS by Mobile Phase Additives. *J. Am. Soc. Mass Spectrom.* **2017,** *28*, 887-894.

39. Gao, X.; Jang, J.; Nagase, S. Hydrazine and Thermal Reduction of Graphene Oxide: Reaction Mechanisms, Product Structures, and Reaction Design. *J. Phys. Chem. C* **2010,** *114*, 832-842.

40. Demarque, D. P.; Crotti, A. E. M.; Vessecchi, R.; Lopes, J. L. C.; Lopes, N. P. Fragmentation reactions using electrospray ionization mass spectrometry: an important tool for the structural elucidation and characterization of synthetic and natural products. *Nat. Prod. Rep.* **2016,** *33*, 432-455.

41. Neta, P.; Simón-Manso, Y.; Liang, Y.; Stein, S. E. Loss of H2 and CO from protonated aldehydes in electrospray ionization mass spectrometry. *Rapid Commun. in Mass Spectrom.* **2014,** *28*, 1871-1882.

42. Moon, I. K.; Lee, J.; Ruoff, R. S.; Lee, H. Reduced graphene oxide by chemical graphitization. *Nat. Commun.* **2010,** *1*, 73.

43. Shin, H.-J.; Kim, K. K.; Benayad, A.; Yoon, S.-M.; Park, H. K.; Jung, I.-S.; Jin, M. H.; Jeong, H.-K.; Kim, J. M.; Choi, J.-Y.; *et al*. Efficient Reduction of Graphite Oxide by Sodium Borohydride and Its Effect on Electrical Conductance. *Adv. Funct. Mater.* **2009,** *19*, 1987-1992.

44. Ambrosi, A.; Pumera, M. Electrochemically Exfoliated Graphene and Graphene Oxide for Energy Storage and Electrochemistry Applications. *Chem. Eur. J.* **2016,** *22*, 153-159.

45. Newman, L.; Lozano, N.; Zhang, M.; Iijima, S.; Yudasaka, M.; Bussy, C.; Kostarelos, K. Hypochlorite degrades 2D graphene oxide sheets faster than 1D oxidised carbon nanotubes and nanohorns. *npj 2D Mat. Appl.* **2017,** *1*, 39.

46. Morgan, K. M.; Ellis, J. A.; Lee, J.; Fulton, A.; Wilson, S. L.; Dupart, P. S.; Dastoori, R. Thermochemical Studies of Epoxides and Related Compounds. *J. Org. Chem.* **2013,** *78*, 4303-4311.

47. Yoon, S.-M.; Kim, S. J.; Shin, H.-J.; Benayad, A.; Choi, S. J.; Kim, K. K.; Kim, S. M.; Park, Y. J.; Kim, G.; Choi, J.-Y.; *et al*. Selective Oxidation on Metallic Carbon Nanotubes by Halogen Oxoanions. *J. Am. Chem. Soc.* **2008,** *130*, 2610-2616.

48. Wu, C.-H. Studies of the equilibrium and thermodynamics of the adsorption of Cu2+ onto as-produced and modified carbon nanotubes. *J. Colloid Interface Sci.* **2007,** *311*, 338-346.

49. de Poorter, B.; Meunier, B. Catalytic epoxidation of aliphatic terminal olefins with sodium hypochlorite. *Tetrahedron Lett.* **1984,** *25*, 1895-1896.

50. Gómez-Navarro, C.; Weitz, R. T.; Bittner, A. M.; Scolari, M.; Mews, A.; Burghard, M.; Kern, K. Electronic Transport Properties of Individual Chemically Reduced Graphene Oxide Sheets. *Nano Lett.* **2007,** *7*, 3499-3503.

51. Feng, H.; Cheng, R.; Zhao, X.; Duan, X.; Li, J. A low-temperature method to produce highly reduced graphene oxide. *Nat. Commun.* **2013,** *4*, 1539.

52. Gao, W.; Alemany, L. B.; Ci, L.; Ajayan, P. M. New insights into the structure and reduction of graphite oxide. *Nat. Chem.* **2009,** *1*, 403-408.

53. Bagri, A.; Mattevi, C.; Acik, M.; Chabal, Y. J.; Chhowalla, M.; Shenoy, V. B. Structural evolution during the reduction of chemically derived graphene oxide. *Nat. Chem.* **2010,** *2*, 581-587.

54. Eda, G.; Lin, Y.-Y.; Mattevi, C.; Yamaguchi, H.; Chen, H.-A.; Chen, I.-S.; Chen, C.-W.; Chhowalla, M. Blue Photoluminescence from Chemically Derived Graphene Oxide. *Adv. Mater.* **2010,** *22*, 505-509.

55. Cox, E. G. The crystalline structure of benzene. *Proc. R. Soc. Lond. A* **1932,** *135*, 491-498.

56. Ruiz-Morales, Y. HOMO−LUMO Gap as an Index of Molecular Size and Structure for Polycyclic Aromatic Hydrocarbons (PAHs) and Asphaltenes: A Theoretical Study. I. *J. Phys. Chem. A* **2002,** *106*, 11283-11308.

57. Adkins, E. M.; Miller, J. H. Towards a taxonomy of topology for polynuclear aromatic hydrocarbons: linking electronic and molecular structure. *Phys. Chem. Chem. Phys.* **2017,** *19*, 28458-28469.

58. Wei, K.; Liao, F.; Huang, H.; Shao, M.; Lin, H.; Liu, Y.; Kang, Z. Simple Semiempirical Method for the Location Determination of HOMO and LUMO of Carbon Dots. *J. Phys. Chem. C* **2021**, *125*, 7451-7457.

59. World Health Organization. Regional Office for, E. *WHO guidelines for indoor air quality: selected pollutants*. WHO Regional Office for Europe: Copenhagen, 2010.

60. Working Group on the Evaluation of Carcinogenic Risks to Humans. Some non-heterocyclic polycyclic aromatic hydrocarbons and some related exposures. In *IARC Monograph Evaluation Carcinogenic Risks Humans*; The International Agency for Research on Cancer: Lyon, **2010,** *92*, 1-853.

61. Bauer, A. K.; Velmurugan, K.; Plöttner, S.; Siegrist, K. J.; Romo, D.; Welge, P.; Brüning, T.; Xiong, K.-N.; Käfferlein, H. U. Environmentally prevalent polycyclic aromatic hydrocarbons can elicit co-carcinogenic properties in an in vitro murine lung epithelial cell model. *Arch. Toxicol.* **2018,** *92*, 1311-1322.

62. Pan, S.; Sardesai, N. P.; Liu, H.; Li, D.; Rusling, J. F. Assessing DNA damage from enzyme-oxidized single-walled carbon nanotubes. *Toxicol. Res.* **2013,** *2*, 375-378.

63. Geier, M. C.; Chlebowski, A. C.; Truong, L.; Massey Simonich, S. L.; Anderson, K. A.; Tanguay, R. L. Comparative developmental toxicity of a comprehensive suite of polycyclic aromatic hydrocarbons. *Arch. Toxicol.* **2018,** *92*, 571-586.

64. Sowada, J.; Lemoine, L.; Schön, K.; Hutzler, C.; Luch, A.; Tralau, T. Toxification of polycyclic aromatic hydrocarbons by commensal bacteria from human skin. *Arch. Toxicol.* **2017,** *91*, 2331-2341.

65. Xue, W.; Warshawsky, D. Metabolic activation of polycyclic and heterocyclic aromatic hydrocarbons and DNA damage: A review. *Toxicol. Appl. Pharmacol.* **2005,** *206*, 73-93.

66. Incardona, J. P.; Day, H. L.; Collier, T. K.; Scholz, N. L. Developmental toxicity of 4-ring polycyclic aromatic hydrocarbons in zebrafish is differentially dependent on AH receptor isoforms and hepatic cytochrome P4501A metabolism. *Toxicol. Appl. Pharmacol.* **2006,** *217*, 308-321.

67. US Department of Health and Human Services. *Toxicological profile for Polycyclic Aromatic Hydrocarbons*; Agency for Toxic Substances and Disease Registry: Atlanta, 1995.

TOC Graphic